A Full-Optical Pretouch Dual-Modal and Dual-Mechanism (PDM^2) Sensor for Robotic Grasping*

Cheng Fang, Zhiyu Yan, Fengzhi Guo, Shuangliang Li, Dezhen Song, and Jun Zou

***Abstract*—We report a new full-optical pretouch dual-modal and dual-mechanism (PDM^2) sensor based on an air-coupled fiber-tip surface micromachined optical ultrasound transducer (SMOUT). Compared to ring-shaped piezoelectric acoustic receivers in previous PDM^2 sensors, the acoustic signal received by the new fiber-tip SMOUT is readout optically, which is naturally resistant to surrounding electromagnetic interference (EMI) and makes the complex grounding and shielding unnecessary. In addition, the new fiber-tip SMOUT receiver has a much smaller size, which makes it possible to further miniaturize the sensor package into a more compact structure. For verification, a prototype of the full-optical PDM^2 sensor has been designed, fabricated, and characterized. The experimental results show that even with the much smaller acoustic receiver, the new sensor can still achieve ranging and material/structure sensing performances comparable with the previous ones. Therefore, the new full optical PDM^2 sensor design is promising in providing a practical and miniaturized solution for ranging and material/structure sensing to assist robotic grasping of unknown objects.**

I. Introduction and Related Work

When robots enter a wide variety of domestic daily applications, a daunting challenge is grasping unknown objects, because the location, shape, subsurface structure, and materials of those objects are often not available [1] [2]. A camera with recently advent deep learning algorithm can provide a lot of context information, but appearance can be deceiving. Without the object information, it is difficult to properly anticipate the friction coefficient, contact characteristics, or force tolerance. Consequently, grasping unknown objects without sensory input is impractical [3] [4], and *in situ* detection is necessary to guarantee robust grasping.

Regrettably, current sensors largely struggle to meet these requirements. For example, regular cameras, RGBD cameras, and laser range finders are challenged by occlusion [5] and blind zone [6] [7] [8] [9] when robotic grippers are too close to objects. Physical contact required by the tactile [10] [11] and force sensors [12] can displace or break the target, resulting in unstable or inefficient grasping. The (contactless) proximity/pretouch sensors based on light, electric field, and sound have been developed recently, but their applications are still limited to a small class of targets because of their sensing mechanisms. Specifically, electric field sensors often fail when the dielectric constants of targets are close to that of air [13] [14] [15] [16]. Optical sensors are unable to handle highly reflective or optically transparent targets [17] [18] [19] [20]. Acoustic sensors are not sensitive to sound-absorbing targets [21] [22] [23] [24]. Unfortunately, many common household items pose these challenges.

To overcome these challenges, we have designed a fingertip mounted near-distance sensor based on pulse-echo ultrasound (US) and optoacoustics (OA) for target distance ranging and material/structure detection [25] [26] [27] [28] [29] [30] [31] [32] [33] [34]. We call this pre-touch dual-modal and dual-mechanism (PDM^2) design. For the US modality, after emitting from a transmitter, the acoustic pulses reflected by the target are captured by an acoustic receiver, both of which are housed inside the PDM^2 sensor (Fig. 1(a)). For the OA modality, upon laser pulse illumination, the acoustic pulses are directly induced from the target surface due to the thermal shock caused by the absorbed laser energy and captured by the same acoustic receiver (Fig. 1(b)). In both modalities, the time of flight of the acoustic signal is used to determine the distance from the target to the sensor, while its frequency spectrum is used to differentiate the target material and/or interior structures.

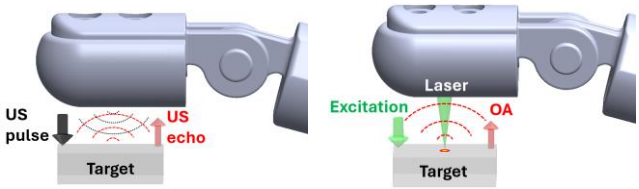

(a) (b)

Figure 1. Illustration of the PDM^2 mechanisms: (a) pulse-echo ultrasound (US), (b) pulsed laser, and induced optoacoustics (OA).

In our previous three generations (G1-G3) of PDM^2 sensor designs ([25] [26] [27] [28] [29] [30] [31] [32] [33] [34]), ring-shaped piezoelectric transducers were used as acoustic receivers to detect US and OA signals without blocking the excitation laser pulses (Figs. 2(a) and 2(b)). However, the piezoelectric transducers and electrical connections are susceptible to the surrounding electromagnetic interference (EMI) that exists widely in real-life situations and thus would require sophisticated grounding and shielding of the sensor package. This is challenging to implement because of the openings on the sensor package that allow sound to pass through. Moreover, the bulky structure of the piezoelectric transducers prevents the sensor from being miniaturized into a compact package for real grasping applications.

*The research is supported in part by the National Science Foundation under ECCS-2330199, CBET-2036134 and NRI-1925037, and by Amazon Research Awards.

C. Fang, Z. Yan, S. Li and J. Zou are with the Electrical and Computer Engineering Department, Texas A&M University, College Station, TX 77843, USA (e-mails: {fangchengok2007, yan1383, slli940922, junzou}@tamu.edu).

F. Guo and D. Song are with the Computer Science and Engineering Department, Texas A&M University, College Station, TX 77843, USA (e-mails: fengzh_g@tamu.edu, dzsong@cs.tamu.edu). D. Song is also with the Robotics Department of Mohamed Bin Zayed University of Artificial Intelligence (MBZUAI), Abu Dhabi, UAE.

Manuscript 500 submitted to 2025 IEEE International Conference on Robotics and Automation (ICRA). Received September 9, 2024.

To address these two issues, this paper reports a new full optical PDM^2 sensor design based on an air-coupled fiber-tip surface micromachined optical ultrasound transducer (SMOUT) [35] [36] [37] [38] as the acoustic receiver (Fig. 2(c)), which is the 4th generation (G4) in the PDM^2 sensor development. The acoustic signal received from the SMOUT is readout optically, which is naturally resistant to EMI, making the complex grounding and shielding unnecessary. Also, the miniaturized size of the SMOUT-based acoustic receiver makes it possible to further reduce the sensor package to a more compact structure. To verify the new design, a prototype of the G4 PDM^2 sensor has been designed, fabricated, and characterized. The experimental results show that even with the much smaller acoustic receiver, the G4 sensor can still achieve ranging and material/structure sensing performances comparable to those of the previous ones. Therefore, the new G4 full-optical PDM^2 sensor design is promising in providing a more practical solution for ranging and material/structure sensing.

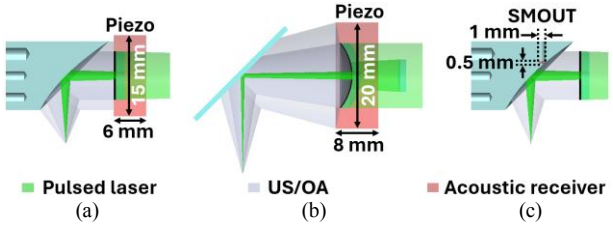

Figure 2. Schematic diagrams showing different PDM^2 sensor designs (a) G1 [27] & G2 [28] [31] [34], (b) G3 [33], and (c) G4 PDM^2 sensors. US: pulse-echo ultrasound; OA: optoacoustics. SMOUT: surface-micromachined optical ultrasound transducer.

II. Sensor Design, Construction and Testing

Fig. 3 shows the schematic design of the G4 full-optical PDM^2 sensor, which comprises an (optoacoustic) ultrasound transmitter [28] [31] [34] and the new fiber-tip SMOUT acoustic receiver. Upon the 532-nm laser pulse delivered through the excitation optical fiber, the ultrasound transmitter (made of black electrical tape laminated onto a clear acrylic substrate [28] [31] [34]) emits a wideband ultrasound pulse towards the target, which is reflected and focused by the parabolic mirror. Simultaneously, the inner part of the laser beam passes through the center hole of the ultrasound transmitter, which is also reflected and focused by the parabolic mirror to the target. Both the US echo and the induced OA signals are received by the fiber-tip SMOUT, whose time-of-flight (ToF) and frequency spectra are used for target distance ranging and material/structure sensing, respectively. It should be mentioned that the US and OA signals triggered by the same laser pulse will not mix with each other because of their different travel paths and times. Specifically, the OA signal will arrive at an earlier time after a single trip from the target surface to the SMOUT, while the US signals go through an almost round trip. A photodetector (PD) detects the laser pulse and generates a trigger signal to synchronize the data acquisition. To readout the ultrasound signal, the fiber-tip SMOUT is interrogated with near-infrared (NIR) continuous-wave (CW) light. Output from an 830-nm laser diode, the light is focused into Port 1 of the circulator and travels through Port 2 to the SMOUT. The light reflected by the SMOUT (modulated by the ultrasound signal [35] [36] [37] [38]) travels back through Ports 2 and 3, and is captured by the second PD, pre-amplified, and recorded by an oscilloscope after 128 averaging.

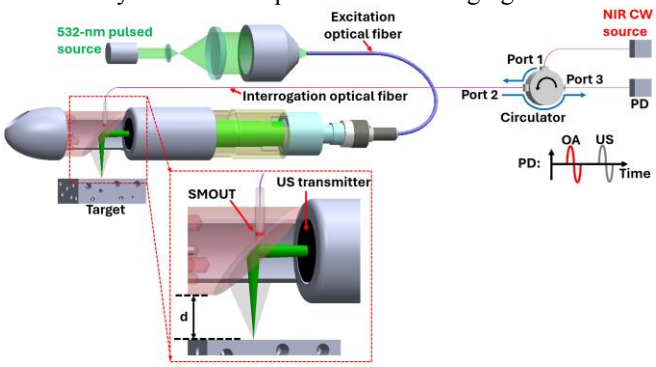

Figure 3. Schematic design of the G4 full-optical PDM^2 sensor with the new fiber-tip SMOUT acoustic receiver. US: pulse-echo ultrasound; OA: optoacoustics; NIR: near-infrared; CW: continuous-wave; PD: photodetector; SMOUT: surface-micromachined optical ultrasound transducer.

Fig. 4(a) shows the schematic design and the acoustic-detection mechanism of the fiber-tip SMOUT acoustic receiver, which is the key component for the full-optical G4 sensor design. Single SMOUTs with a diameter (ϕ) of 300 μm are first fabricated on a 0.5-mm-thick glass substrate and then diced into individual 1.0×1.0 mm^2 chips, which are much smaller than the previous ring-shaped piezoelectric receivers with typical diameters of 15~20 mm. Each SMOUT consists of an interferometric Fabry-Perot (F-P) cavity (with optical resonance wavelength λ_0) formed by two (top and bottom) distributed Bragg reflectors (DBRs). As the ultrasound waves impinge on the SMOUT, the flexible top DBR diaphragm vibrates and thus shifts the optical reflectivity spectrum of the F-P cavity (Fig. 4(b)). As a result, the amplitude of light reflected by the SMOUT is modulated by the sound pressure. The middle point of the slope of reflectivity spectrum (λ_{bias}) is selected as the wavelength of the light source to interrogate the SMOUT to provide maximal linearity and dynamic range of the output signal [35] [36] [37] [38]. A single SMOUT element is mounted on the tip of a multimode optical fiber (ϕ_{core} = 200 μm) by ultraviolet (UV) epoxy, which is supported by a ceramic ferrule (ϕ_{outer} = 1.25 mm, ϕ_{inner} = 230 μm). A 3D-printed tubing is attached to the ferrule to protect the fiber from overbending and breaking. Fig. 4(c) shows a fabricated prototype of the fiber-tip SMOUT acoustic receiver.

Because SMOUTs do not have sending capability, a transmitting-receiving setup is built for quick estimation of the acoustic reception bandwidth of the fiber-tip SMOUT (Fig. 5(a)). Driven by a pulser-receiver, ultrasound pulses are transmitted from different air-coupled (narrowband) ultrasound transducers with 0.1-, 0.2-, 0.4-, 1-, and 2-MHz center frequencies (f_c) to the fiber-tip SMOUT. After 40-dB pre-amplification, the f_c and peak-to-peak amplitude (V_{pp}) of the SMOUT-received signals vs. transmitter f_c are plotted in Figs. 5(b) and 5(c), respectively. The results indicate that the acoustic reception bandwidth of the fiber-tip SMOUT can cover the frequency range of 0.1 to 2 MHz. The V_{pp} variation may be caused by the different acoustic intensities

Manuscript 500 submitted to 2025 IEEE International Conference on Robotics and Automation (ICRA). Received September 9, 2024.

transmitted from the air-coupled transducers with different f_c.

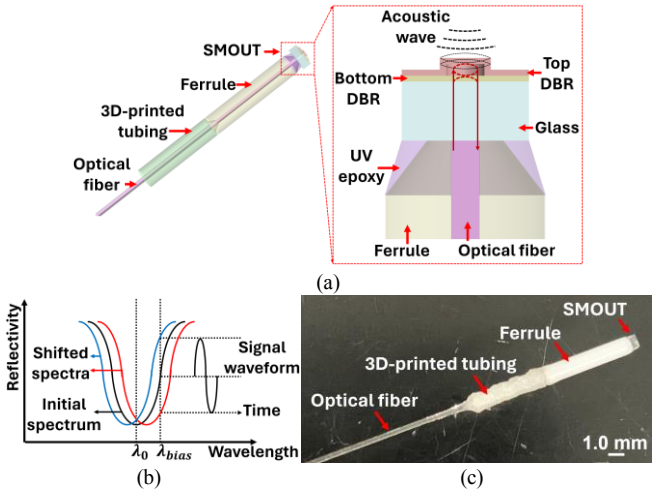

Figure 4. (a) Schematic design and the acoustic-detection mechanism of the fiber-tip SMOUT acoustic receiver. DBR: distributed Bragg reflector. UV: ultraviolet. (b) The reflectivity spectrum of the SMOUT shifted by the impinging ultrasound, which modulates the optical reflectivity at the interrogation wavelength λ_{bias}. (c) A photo of the fabricated fiber-tip SMOUT acoustic receiver, consisting of a signle SMOUT element, ceramic ferrule, 3D-printed tubing, and the interrogation optical fiber.

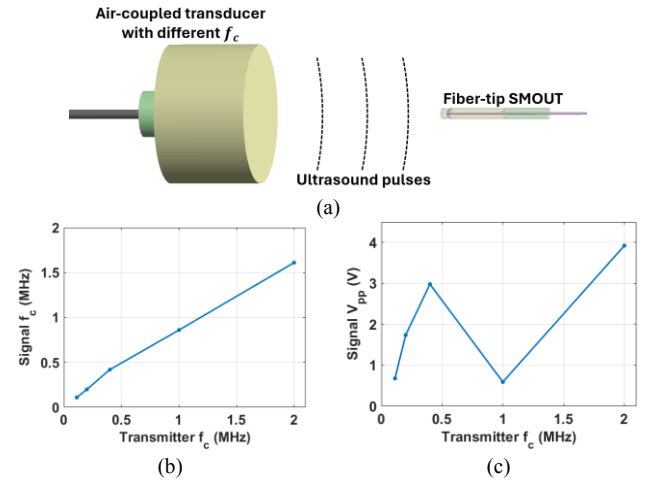

Figure 5. (a) Schematic diagram of the transmitting-receiving setup with air-coupled transducers with 0.1-, 0.2-, 0.4-, 1-, and 2-MHz f_c to characterize the acoustic reception bandwidth of the fiber-tip SMOUT. The (b) f_c and (c) V_{pp} of the SMOUT-received signals vs. different f_c of the air-coupled ultrasound transmitters.

Fig. 6(a) shows a photograph of the fabricated prototype of the G4 sensor, which consists of a 3D-printed housing, a fiber-tip SMOUT, a 90-degree parabolic mirror, a flat (optoacoustic) ultrasound transmitter, a 3D-printed coupler, a fiber collimator, and an excitation optical fiber. A Q-switched 532-nm Nd:YAG pulsed laser is used as the light source to excite both US and OA signals, which has a 10-Hz repetition rate, an 8-ns pulse duration, and 20-mJ average pulse energy. The laser pulse energy is attenuated by a neutral density filter to around 2.5 mJ to protect the black tape layer (the OA medium of the ultrasound transmitter) from photobleaching. The pulsed laser beam is expanded by two lenses and then focused on the excitation optical fiber with ϕ = 1 mm. The fiber-tip SMOUT is inserted into a 1.6-mm-ϕ hole drilled through the parabolic mirror. The hole is offset from the laser reflection area, and its diameter is much smaller than the ultrasound beam. Therefore, it has minimal impact on the optical and acoustic reflection and focusing of the parabolic mirror. A representative dual-modal signal from an aluminum block is shown in Fig. 6(b), which consists of both OA and US signals initiated by one laser pulse. The time delays for the first OA signal, the echo US signal, and the second OA signal (echo after a round trip) are around 43.3 µs, 106.4 µs, and 168.7 µs, respectively. The temporal separations of the US and OA signals are large enough to isolate them from each other.

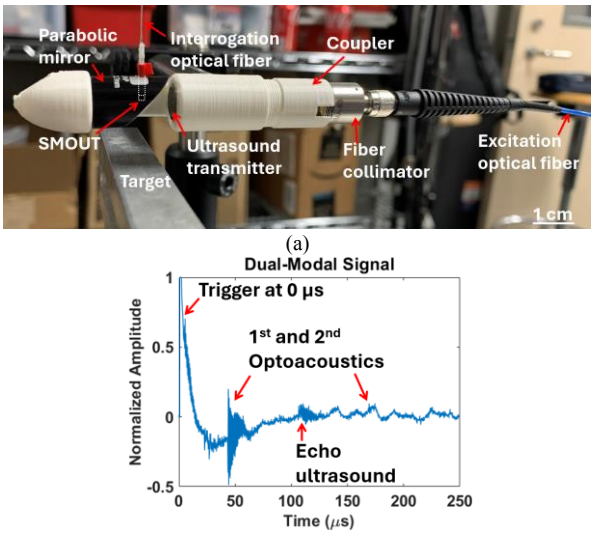

Figure 6. (a) Photograph of the prototype fabricated from the G4 sensor. (b) Representative dual-modal signal received by the G4 sensor from an aluminum block through air.

Table I lists and compares the total volume of the acoustic receiver, the overall dimensions, and the potential for further miniaturization of all PDM^2 sensor designs. Especially with a much smaller acoustic receiver, the G4 sensor can be easily further miniaturized by using an ultrasound transmitter and a parabolic mirror with smaller diameters.

TABLE I. COMPARISON OF PDM^2 SENSORS IN OVERALL DIMENSIONS AND POTENTIAL FOR FURTHER MINIATURIZATION

	G1 [27]	G2 [31]	G3 [33]	G4
Total volume of acoustic receiver (mm^3)	1060	1060	2513	0.5
Overall diameter (mm)	21.0	21.0	26.0	15.0
Potential for further miniaturization	Low	Low	Low	High

III. RANGING EXPERIMENT AND RESULTS

A. Pulse-echo Ultrasound Distance Ranging

The US ranging performance of the G4 sensor is characterized by using a 1mm thick glass slide as the target. The distance (d) between the parabolic mirror and the glass slide is decreased from 15.0 mm to 2.0 mm with a decrement of 0.5 mm. The measured vs. actual distance (d) and their deviations are shown in Figs. 7(a) and 7(b), respectively. The raw deviations are up to 2.7 mm when d is 15.0 mm (far out

of the focal zone). To reduce the deviation outside the focal zone and improve the effective working distance, the raw deviation (black curve) is fitted and then subtracted by a second-order polynomial curve (red curve) for rectification (Fig. 7(b)). The rectified deviation (blue curve) is less than 0.10 mm, where d is from 2.0 mm to 15.0 mm. The same setup is used to quantify the lateral resolution of the US ranging, except that the glass slide is replaced by a 1.0-mm-ϕ optical fiber. The fiber is scanned laterally, and the recorded US profile is fitted by a Gaussian curve, whose FWHM (full width at half maximum) is used to determine the US focal diameter (ϕ). After repeating the lateral scans at different distance (d) from 2.0 mm to 15.0 mm, the US lateral resolution is determined by the minimal US focal diameter (Fig. 7(c)), which is around 0.92 mm at the focal length d = 6.5 mm. The measured focal zone is around 7.0 mm, where d changes from 3.0 mm to 10.0 mm.

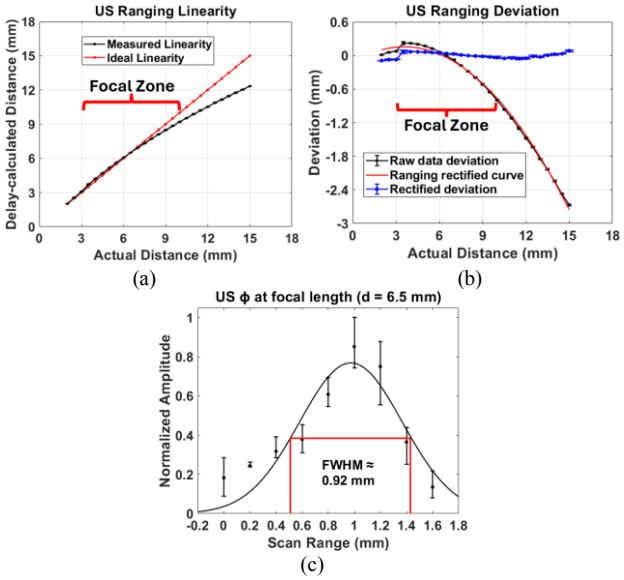

Figure 7. (a) Comparison between the US measured (in black) and actual (in red) distances. (b) Deviation of the US measured distance from the actual distance. (c) US lateral resolution of 0.92 mm determined by the minimal US focal diameter at d = 6.5 mm.

B. *Optoacoustic Distance Ranging*

The OA ranging performance of the G4 sensor is characterized by using an aluminum block as the target. The distance (d) between the parabolic mirror and the aluminum block is decreased from 20.0 mm to 0.0 mm with a decrement of 0.5 mm. The measured vs. the actual distance (d) and their deviations are shown in Figs. 8(a) and 8(b), respectively. Again, after fitting and rectification by a second-order polynomial curve, the deviation is reduced to less than 0.2 mm, where d is between 0.0 mm to 20.0 mm. The same setup is used to quantify the OA lateral resolution, except that the aluminum block is replaced by a pencil lead with ϕ = 0.36 mm. The pencil lead is scanned laterally and the recorded OA profile is fitted with a Gaussian curve, whose FWHM is used to determine the focal diameter (ϕ). After repeating the lateral scans at different distances (d) from 0.0 mm to 20.0 mm, the OA lateral resolution is determined by the minimal OA focal diameter (Fig. 8(c)), which is around 0.45 mm at the focal length d = 9.5 mm. The measured focal zone is around 9.0 mm, where d changes from 5.0 mm to 14.0 mm.

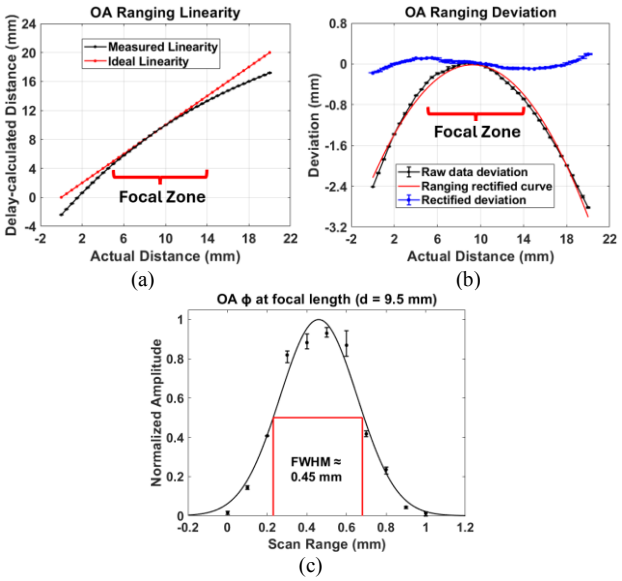

Figure 8. (a) Comparison between the OA measured (in black) and the actual (in red) distances. (b) Deviation of the OA measured distance from the actual distance. (c) OA lateral resolution of 0.45 mm determined by the minimal OA focal diameter at d = 9.5 mm.

Table II lists and compares the ranging performances of all PDM^2 sensors. Among them, the G3 sensor has the best overall performance. Note that this is mainly due to its more complex optical and acoustic focusing and reflection mechanism. As shown in Fig. 2(b), the laser pulses are focused by a small convex lens inside the package, while the ultrasound focusing is achieved by the specially-designed and molded concave shape of the transmitter. The focused laser and ultrasound beams are reflected by a 45º flat mirror plate onto the target. Due to this, the G3 sensor is also the bulkiest. In contrast, the G1, G2 and G4 sensors share the same optical and acoustic focusing and reflection mechanism with a single right-angle parabolic mirror for both focusing and reflection (Figs. 2(a) and 2(c)). From Table II, it can be concluded that even with the much smaller fiber-tip SMOUT acoustic receiver, the G4 sensor can still achieve comparable US and OA ranging performances with the G1 and G2 sensors.

TABLE II. RANGING PERFORMANCE COMPARISON OF PDM^2 SENSORS

Ranging Performances	G1 [27]	G2 [31]	G3 [33]	G4
US Focal Zone (mm)	2.0	4.5	10 .0	7.0
US Max Deviation within the Focal Zone (mm)	0.24	0.20	0.10	0.10
US Lateral Resolution (mm)	1.04	0.75	1.04	0.92
US Effective Working Range (mm)	2.0	12.0	70.0*	13.0
OA Focal Zone (mm)	1.0	4.0	50*	9.0
OA Max Deviation within Focal Zone (mm)	0.12	0.16	0.13	0.20
OA Lateral Resolution (µm)	95.0	392.0	290.0	450.0
OA Effective Working Range (mm)	2.0	12.0	70.0*	20.0
Overlap of US/OA focal zone (mm)	0.0	4.0	10.0	5.0

* Based on a different focusing and reflection mechanism.

IV. Material Sensing Experiment and Results

A. Data Acquisition and Classification

In addition to ranging the target distance, the induced OA and/or US echo signals are also utilized to interrogate the material/subsurface structure (especially the thickness) of the target. The testing setup is similar to that shown in Fig. 6(a) and the captured waveforms are similar to that shown in Fig. 6(b). Due to the different thicknesses of the target, the height of the target is adjusted by the supporting Z-axis stage to maintain the same target-to-sensor distance d = 8 mm. OA and US signals consist of distinctive features of the optical and mechanical properties of targets, which can be differentiated by a machine learning-based classifier, such as Bag-of-SFA symbols (BOSS) [39] [40]. Fifteen waveforms are collected from each target, which is preprocessed and randomly divided into training and testing groups with a ratio of 11:4 without overlap. After 50 random trials, the confusion matrix is generated to show the accuracy of the classification.

B. Material/Thickness Differentiation

The performance of the G4 sensor in differentiating target material/subsurface structure (thickness) is characterized by four common household materials, including acrylic, aluminum block, thick white paper, and black rubber, as well as four aluminum sheets with different thicknesses of 0.02-, 0.27-, 1.57-, and 6.35-mm. Representative acoustic spectra of different materials and thickness are shown in Figs. 9 and 10, respectively. The confusion matrices given by the BOSS classifier (Fig. 11) indicate an overall ≥ 99.5% accuracy of material differentiation and an overall ≥ 96.5% accuracy of thickness classification, which are similar to those obtained with previous sensors [27] [28] [31].

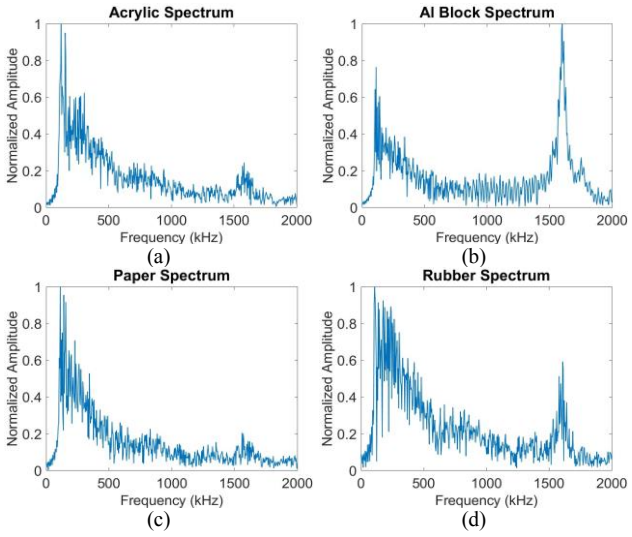

Figure 9. Representative OA-US frequency spectra from four common household materials: (a) acrylic, (b) aluminum block, (c) thick white paper, and (d) rubber. Al: aluminum.

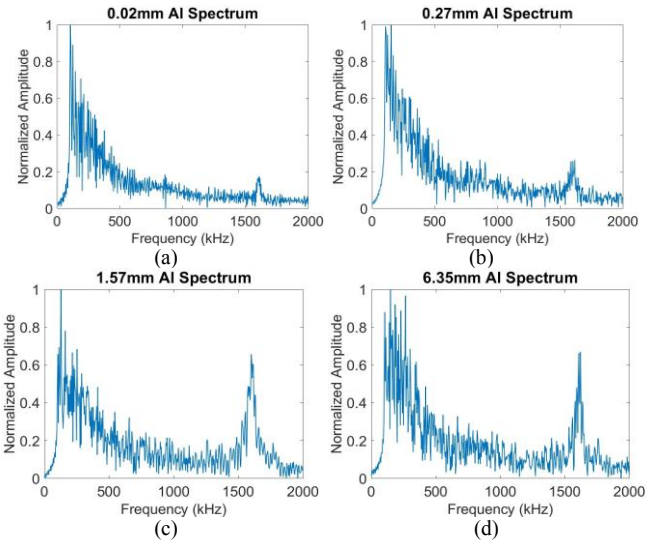

Figure 10. Representative OA-US frequency spectra from aluminum sheets with four different thickness. Al: aluminum.

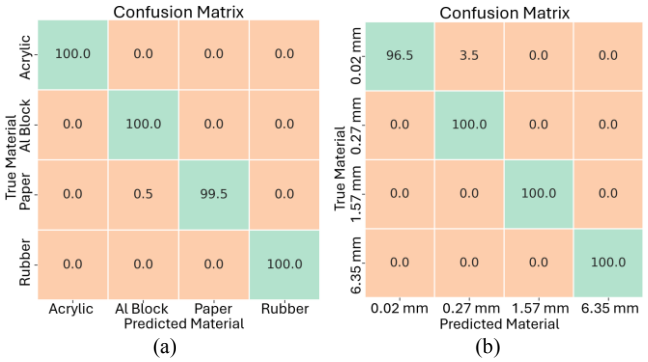

Fig. 11. BOSS classifier averaged confusion matrix of (a) four common household materials and (b) aluminum sheets with four different thicknesses. Al: aluminum.

C. Differentiation of Challenging Targets

Besides the normal targets, the differentiation capabilities of the G4 sensor are further investigated by the six optical and acoustic challenging targets (OACTs) (Fig. 12), including four dark thin/porous targets of fabric, foam, paper, window tint film (Figs. 12(a)-(d)) (with weak acoustic reflection), and two optically-transparent targets of glass and PET (polyethylene terephthalate) (Figs. 12(e)-(f)) with low optical absorption. The confusion matrix provided by the BOSS classifier (Fig. 12(g)) indicates an overall ≥ 96% accuracy for all targets except paper vs. foam with somewhat similar mechanical properties. With low-cost construction, there are random fluctuations in the optical output power of the 830-nm laser diode, which results in lower repeatability of acquired signals. This makes data averaging less effective in noise reduction, because useful signals can also be smoothed out. The lower signal-to-noise ratio (SNR) could reduce the accuracy of the classification of similar materials and structures.

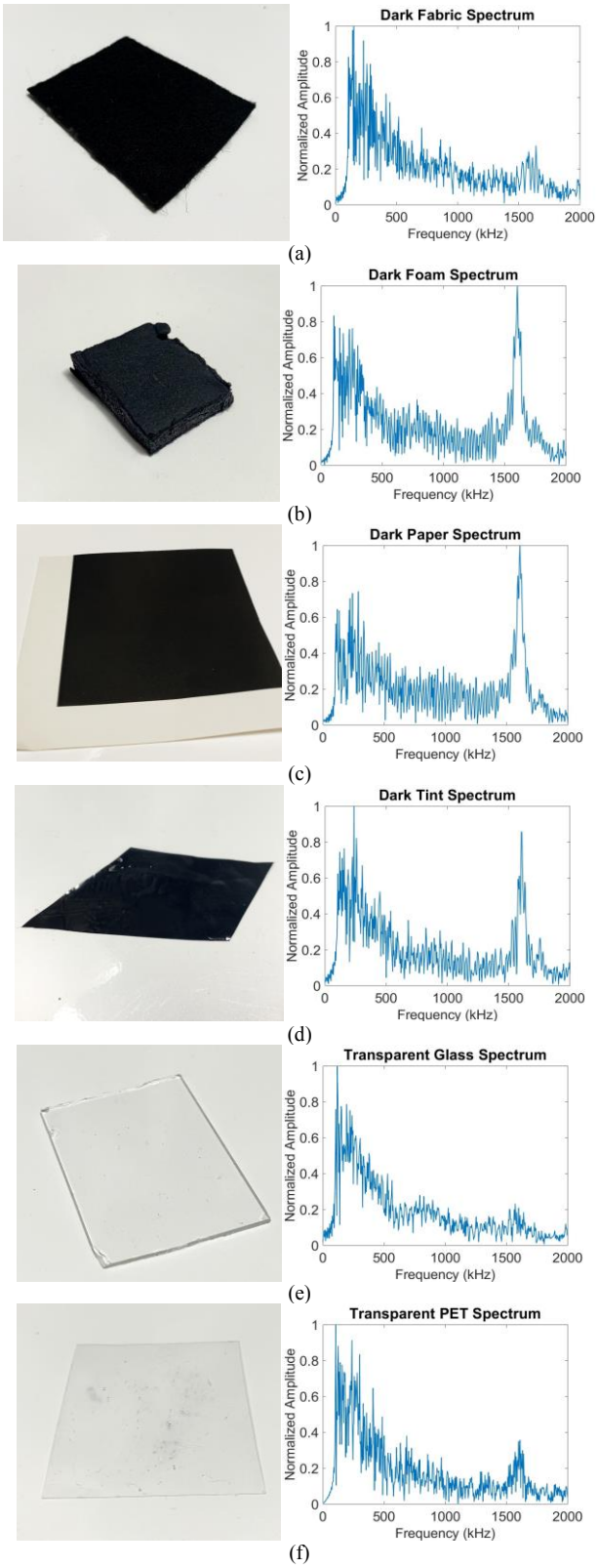

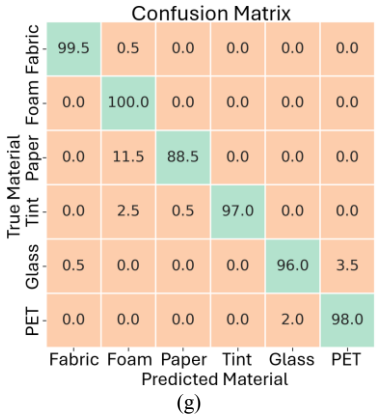

Figure 12. Photographs and representative OA-US frequency spectra of (a-d) dark thin/porous targets of fabric, foam, paper, window tint film with thicknesses around 2 mm, 5 mm, 0.1 mm, 0.06 mm, respectively, and (e-f) optically-transparent targets of glass and PET with thicknesses around 1.0 mm, 0.11 mm, respectively. (g) BOSS classifier averaged confusion matrix of the six OACTs.

V. Conclusion and Future Work

A new (G4) full-optical PDM^2 sensor has been demonstrated for near-distance US and OA ranging and material/structure sensing for robotic grasping. By using a fiber-tip SMOUT to replace the previous ring-shaped piezoelectric transducer as the acoustic receiver, the G4 sensor can achieve ranging and sensing performances comparable to previous sensors, as well as natural resistance to EMI because of its full optical design. In addition, it allows further miniaturization of the sensor package. These two features make it a more practical pretouch sensing solution for optimizing robotic grasping of unknown objects in challenging environments. In the future, the power instability of the interrogation light source will be addressed, and the sensor package will be further miniaturized to facilitate mounting on robotic arms [31] [34]for faster and more flexible scanning.

Acknowledgment

The authors would like to thank for the inputs and feedback from Di Wang.

References

[1] M. T. Mason, Mechanics of Robotic Manipulation, MIT press, 2001.

[2] M. Ciocarlie, K. Hsiao, E.G. Jones, S. Chitta, R.B. Rusu and I.A. Şucan, "Towards reliable grasping and manipulation in household environments," *Experimental Robotics,* pp. 241-252, Springer, Berlin, Heidelberg, 2014.

[3] K. Y. Goldberg, "Orienting Polygonal Parts Without Sensors," *Algorithmica,* vol. 10, no. 2-4, pp. 201-225, 1993.

[4] M. A. Erdmann and M. T. Mason, "An exploration of sensorless manipulation," *IEEE Journal on Robotics and Automation,* vol. 4, no. 4, pp. 369-379, 1988.

[5] C. E. Smith and N. P. Papanikolopoulos, "Vision-Guided Robotic Grasping: Issues and Experiments," *Proceedings of IEEE International Conference on Robotics and Automation,* vol. 4, pp. 3203-3208, 1996.

[6] A. Wehr and U. Lohr, "Airborne laser scanning—an introduction and overview," *ISPRS Journal of photogrammetry and remote sensing,* vol. 54, no. 2-3, pp. 68-82, 1999.

[7] Y. Lu, J. Lee, S. H. Yeh, H. M. Cheng, B. Chen and D. Song, "Sharing Heterogeneous Spatial Knowledge: Map Fusion between Asynchronous Monocular Vision and Lidar or Other Prior Inputs,"

Robotics Research, pp. 727-741, Springer, Cham, 2020.

[8] M. C. Amann, T. M. Bosch, M. Lescure, R. A. Myllylae and M. Rioux, "Laser ranging: a critical review of unusual techniques for distance measurement," *Optical engineering,* vol. 40, pp. 10-19, 2001.

[9] A. Stelzer, M. Jahn and S. Scheiblhofer, "Precise distance measurement with cooperative FMCW radar units," *In 2008 IEEE Radio and Wireless Symposium,* pp. 771-774, 2008.

[10] R. D. Howe, "Tactile sensing and control of robotic manipulation," *Advanced Robotics,* vol. 8, no. 3, pp. 245-261, 1993.

[11] J. M. Romano, K. Hsiao, G. Niemeyer, S. Chitta and K. J. Kuchenbecker, "Human-Inspired Robotic Grasp Control With Tactile Sensing," *IEEE Transactions on Robotics,* vol. 27, no. 6, pp. 1067-1079, 2011.

[12] Q. Xu, "Design and Development of a Novel Compliant Gripper With Integrated Position and Grasping/Interaction Force Sensing," *IEEE Transactions on Automation Science and Engineering,* vol. 14, no. 3, pp. 1415 - 1428, 2015.

[13] J. R. Smith, E. Garcia, R. Wistort and G. Krishnamoorthy, "Electric field imaging pretouch for robotic graspers," *In 2007 IEEE/RSJ International Conference on Intelligent Robots and Systems,* pp. 676-683, 2007.

[14] R. Wistort and J. R. Smith, "Electric field servoing for robotic manipulation," *In 2008 IEEE/RSJ International Conference on Intelligent Robots and Systems,* pp. 494-499, 2008, September.

[15] B. Mayton, L. LeGrand and J. R. Smith, "An electric field pretouch system for grasping and co-manipulation," *In 2010 IEEE International Conference on Robotics and Automation,* pp. 831-838, 2010.

[16] B. Mayton, E. Garcia, L. LeGrand and J. R. Smith, "Electric field pretouch: Towards mobile manipulation," *In RSS Workshop on Mobile Manipulation in Human Environments,* 2009, June.

[17] K. Hsiao, P. Nangeroni, M. Huber, A. Saxena and A. Y. Ng, "Reactive grasping using optical proximity sensors," *In 2009 IEEE International Conference on Robotics and Automation,* pp. 2098-2105, 2009.

[18] B. Yang, P. Lancaster and J. R. Smith, "Pre-touch sensing for sequential manipulation," *In 2017 IEEE International Conference on Robotics and Automation (ICRA),* pp. 5088-5095, 2017.

[19] H. Hasegawa, Y. Mizoguchi, K. Tadakuma, A. Ming, M. Ishikawa and M. Shimojo, "Development of intelligent robot hand using proximity, contact and slip sensing," *In 2010 IEEE International Conference on Robotics and Automation,* pp. 777-784, 2010, May.

[20] A. Maldonado, H. Alvarez and M. Beetz, "Improving robot manipulation through fingertip perception," *In 2012 IEEE/RSJ International Conference on Intelligent Robots and Systems,* pp. 2947-2954, 2012.

[21] L. T. Jiang and J. R. Smith, "A unified framework for grasping and shape acquisition via pretouch sensing," *In 2013 IEEE International Conference on Robotics and Automation,* pp. 999-1005, 2013, May.

[22] E. Guglielmelli, V. Genovese, P. Dario and G. Morana, "Avoiding obstacles by using a proximity US/IR sensitive skin," *In Proceedings of 1993 IEEE/RSJ International Conference on Intelligent Robots and Systems (IROS'93),* vol. 3, pp. 2207-2214, 1993, July.

[23] L. T. Jiang and J. R. Smith, "Seashell effect pretouch sensing for robotic grasping," *In 2012 IEEE International Conference on Robotics and Automation,* pp. 2851-2858, 2012, May.

[24] L. T. Jiang and J. R. Smith, "Pretouch sensing for manipulation," *In Robotics: Science and Systems (RSS) Workshop: Alternative Sensing Techniques for Robotic Perception,* 2012, July.

[25] C. Fang, D. Wang, D. Song and J. Zou, "Toward Fingertip Non-Contact Material Recognition and Near-Distance Ranging for Robotic Grasping," *International Conference on Robotics and Automation (ICRA), IEEE,* pp. 4967-4974, 2019, May.

[26] C. Fang, D. Wang, D. Song and J. Zou, "Fingertip Non-Contact Optoacoustic Sensor for Near-Distance Ranging and Thickness Differentiation for Robotic Grasping," *In 2020 IEEE/RSJ International Conference on Intelligent Robots and Systems (IROS),* pp. 10894-10899, IEEE, 2020.

[27] C. Fang, D. Wang, D. Song and J. Zou, "Fingertip Pulse-Echo Ultrasound and Optoacoustic Dual-Modal and Dual Sensing Mechanisms Near-Distance Sensor for Ranging and Material Sensing in Robotic Grasping," *In 2021 IEEE International Conference on Robotics and Automation (ICRA) ,* pp. 14105-14111, 2021.

[28] C. Fang, D. Wang, D. Song and J. Zou, "The Second Generation (G2) Fingertip Sensor for Near-Distance Ranging and Material Sensing in Robotic Grasping," *In IEEE 2022 International Conference on Robotics and Automation (ICRA),* pp. 1506-1512, 2022, May.

[29] D. Wang, F. Guo, C. Fang, J. Zou and D. Song, "Design of an Object Scanning System and a Calibration Method for a Fingertip-Mounted Dual-Modal and Dual Sensing Mechanisms (DMDSM)-based Pretouch Sensor for Grasping," *In 2022 IEEE 18th International Conference on Automation Science and Engineering (CASE),* pp. 341-347, 2022, August.

[30] F. Guo, S. Xie, D. Wang, C. Fang, J. Zou and D. Song, "A Pretouch Perception Algorithm for Object Material and Structure Mapping to Assist Grasp and Manipulation Using a DMDSM Sensor," *In 2023 IEEE/RSJ International Conference on Intelligent Robots and Systems (IROS),* 2023.

[31] C. Fang, D. Wang, F. Guo, J. Zou and D. Song, "A Fingertip Sensor and Algorithms for Pre-touch Distance Ranging and Material Detection in Robotic Grasping," *arXiv preprint arXiv:2311.10453,* 2023.

[32] C. Fang, "Dual-Modal and Dual-Sensing-Mechanism (DMDSM) Acoustic Sensors for Robotic Ranging and Material Differentiation," *Doctoral dissertation, Texas A&M University,* 2023.

[33] C. Fang, S. Li, D. Wang, F. Guo, D. Song and J. Zou, "The Third Generation (G3) Dual-Modal and Dual Sensing Mechanisms (DMDSM) Pretouch Sensor for Robotic Grasping," *In 2023 IEEE International Conference on Robotics and Automation (ICRA),* pp. 1731-1736, 2023. IEEE.

[34] F. Guo, S. Xie, D. Wang, C. Fang, J. Zou and D. Song, "Heterogeneous Sensor Fusion and Active Perception for Transparent Object Reconstruction with a PDM² sensor and a Camera," in *(submitted to) IEEE International Conference on Robotics and Automation*, Atlanta, USA, May 19-23, 2025.

[35] Z. Yan and J. Zou, "Large-scale surface-micromachined optical ultrasound transducer (SMOUT) array for photoacoustic computed tomography," *Optics Express,* vol. 30, no. 11, pp. 19069-19080, 2022.

[36] Z. Yan and J. Zou, "Integration of microlenses on surface-micromachined optical ultrasound transducer array to improve detection sensitivity for parallel data readout," *Optics Letters,* vol. 48, no. 3, pp. 652-655, 2023.

[37] Z. Yan and J. Zou, "High-frequency surface-micromachined optical ultrasound transducer array for 3D micro photoacoustic computed tomography," *Optics Letters,* vol. 49, no. 5, pp. 1181-1184, 2024.

[38] Z. Yan, C. Fang and J. Zou, "Fine-Tuning of Optical Resonance Wavelength of Surface-Micromachined Optical Ultrasound Transducer Arrays for Single-Wavelength Light Source Readout," *Micromachines,* vol. 15, no. 9, p. 1111, 2024 Aug 31.

[39] P. Schäfer, "The BOSS is concerned with time series classification in the presence of noise," *Data Mining and Knowledge Discovery,* vol. 29, no. 6, pp. 1505-1530, 2015.

[40] A. Bagnall, J. Lines, A. Bostrom, J. Large and E. Keogh, "The great time series classification bake off: a review and experimental evaluation of recent algorithmic advances," *Data Mining and Knowledge Discovery,* vol. 31, no. 3, pp. 606-660, 2017.